

3D Fast Automatic Segmentation of Kidney Based on Modified AAM and Random Forest

Chao Jin, Fei Shi, Dehui Xiang, Xueqing Jiang, Bin Zhang, Ximing Wang, Weifang Zhu, Enting Gao, and Xinjian Chen*, *Senior Member, IEEE*

Abstract—In this paper, a fully automatic method is proposed to segment the kidney into multiple components: renal cortex, renal column, renal medulla and renal pelvis, in clinical 3D CT abdominal images. The proposed fast automatic segmentation method of kidney consists of two main parts: localization of renal cortex and segmentation of kidney components. In the localization of renal cortex phase, a method which fully combines 3D Generalized Hough Transform (GHT) and 3D Active Appearance Models (AAM) is applied to localize the renal cortex. In the segmentation of kidney components phase, a modified Random Forests (RF) method is proposed to segment the kidney into four components based on the result from localization phase. During the implementation, a multithreading technology is applied to speed up the segmentation process. The proposed method was evaluated on a clinical abdomen CT data set, including 37 contrast-enhanced volume data using leave-one-out strategy. The overall true-positive volume fraction and false-positive volume fraction were 93.15%, 0.37% for renal cortex segmentation; 83.09%, 0.97% for renal column segmentation; 81.92%, 0.55% for renal medulla segmentation; and 80.28%, 0.30% for renal pelvis segmentation, respectively. The average computational time of segmenting kidney into four components took 20 seconds.

Index Terms—Active appearance models, generalized Hough transform, kidney, random forests, renal column, renal cortex, renal medulla, renal pelvis.

I. INTRODUCTION

THE kidney participates in whole-body homeostasis, regulating acid-base balance, electrolyte concentrations, extracellular fluid volume, and blood pressure. According to a

Manuscript received November 19, 2015; accepted December 21, 2015. Date of publication January 05, 2016; date of current version May 28, 2016. This work has been supported in part by the National Basic Research Program of China (973 Program) under Grant 2014CB748600, and in part by the National Natural Science Foundation of China (NSFC) under Grant 81371629, 61401293, 61401294, 81401451, 81401472, and in part by Natural Science Foundation of the Jiangsu Province under Grant BK20140052. *Asterisk indicates corresponding author.*

C. Jin, F. Shi, D. Xiang, X. Jiang, W. Zhu, and E. Gao are with the School of Electronic and Information Engineering, Soochow University, Suzhou 215006, China (e-mail: jking_c2011@163.com; shifei@suda.edu.cn; xiangdehui@suda.edu.cn; jiangxq308@foxmail.com; wfzhu@suda.edu.cn; entinggao@foxmail.com).

X. Wang and B. Zhang are with the First Affiliated Hospital of Soochow University, Suzhou 215006, China (e-mail: wangximing1998@163.com; zbnucmd@126.com).

*X. Chen is with the School of Electronic and Information Engineering, Soochow University, Suzhou 215006, China (e-mail: xjchen@suda.edu.cn).

Color versions of one or more of the figures in this paper are available online at <http://ieeexplore.ieee.org>.

Digital Object Identifier 10.1109/TMI.2015.2512606

survey conducted by the National Institute of Health in 2011, the number of non-institutionalized adults with diagnosed kidney disease is 4.4 million (1.9%) in the USA [1], the number of deaths from nephritis, nephrotic syndrome, and nephrosis is 50,476 [2]. Kidney is consisted of four different structures with different functions, i.e., renal cortex, renal column, renal medulla and renal pelvis [3]. Different kidney diseases affect different part of kidney. For example, kidney tumor [4] usually occurs in renal cortex, renal column hypertrophy [5] may exist in renal column, medullary cystic kidney disease [6] usually exists in renal medulla, and transitional cell cancer, renal pelvis and ureter cancer [7] may attack renal pelvis. Moreover, volume changes of different component may indicate change of different renal functions [8]. The renal cortical volume and thickness have been proven to be effective biomarkers for renal function in many clinical situations [9]–[12]. The volumetry of renal cortex and renal medulla was highly interesting for epidemiological studies [8], [13]. Renal pelvis volume calculation is very important in diagnosing children renal pelvis disease [14]. Especially in community medicine and epidemiological studies, large amount of image data need to be processed. Therefore, automatic, accurate and efficient segmentation of kidney components has great clinical values for the diagnosis and treatment of the kidney diseases, and for renal function and morphological assessment [26].

However, kidney components segmentation is a challenging task due to the following reasons: (1) the anatomical structures of kidney are complex, which consists of four major structures: renal cortex, renal column, renal medulla and renal pelvis, as shown in Fig. 1; (2) the renal cortex and renal column are connected and have similar intensity; (3) the renal pelvis consists of several different structures with different intensities. (4) the boundaries between kidneys and adjacent organs such as spleen and liver are usually blurred.

There were several prior investigations [15]–[27] in kidney and renal cortex segmentation in CT, MRI and Ultrasound images, including both semi-automatic [15]–[18] and fully automatic [19]–[27] methods. Freiman *et al.* [19], Ali *et al.* [21] and Chen *et al.* [25] applied graph cut based method. Xie *et al.* [23] segmented kidney from Ultrasound images based on shape and texture priors. For kidney segmentation in dynamic MR images, not only the spatial information but also the timing activities, also known as time intensity curves, were used for kidney segmentation [17], [22]. Cuingnet *et al.* [24] used Random Forests to detect and segment kidneys in 3D CT images. Recently, Will *et al.* [26] applied threshold and shape detection based algorithm, Yang [27] applied Maximally Stable Temporal Volume

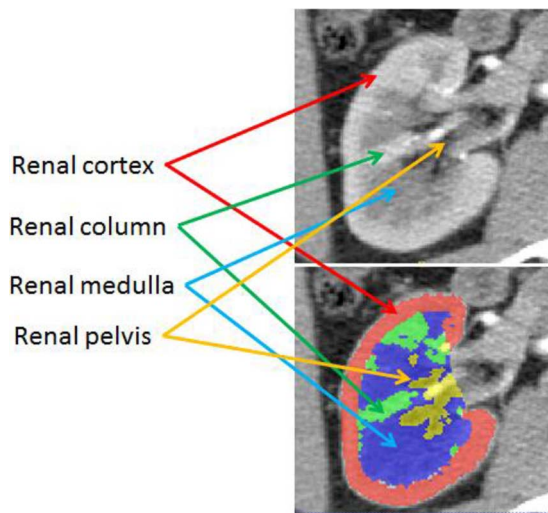


Fig. 1. Anatomy of renal cortex.

(MSTV) and principal components (PCs) based method to segment kidney into three parts (renal cortex, renal medulla and renal pelvis) based on MRI. The studies described above classified cortex and column into one category since they have similar high intensities. However, for precise measurement of the renal cortex thickness, it would be more accurate to consider only the out-layer of the kidney as the cortex and the rest as the column. Chen *et al.* [25] proposed an automatic method for renal cortex segmentation based on oriented active appearance model (OAAM) and graph cut.

In this paper, we propose a fast fully automatic kidney segmentation method which can segment the kidney into four components: renal cortex, renal column, renal pelvis and renal medulla. Two datasets were used in this paper. Dataset 1 was acquired from subjects who donated their left kidney. By this method, the volume change of the four renal components of the remaining kidney before and after donation is analyzed. It is essential for kidney function evaluation [11], [25], [28], [29]. Dataset 2 was acquired from a completely different CT system for both normal subjects and abnormal subjects. Dataset 2 was used to validate the robustness of the proposed method. To the best of our knowledge, this study is the first work that segments the kidney into four components.

The proposed method consists of two parts: localization of renal cortex and segmentation of kidney components. In localization of renal cortex, the Active Appearance Model (AAM) method is used [30]. The AAM is widely used in computer vision such as face recognition [31] and organ localization. Mitchell *et al.* [32] extended the AAM to three dimensions and tested it on Cardiac MR and Ultrasound Images. However, conventional AAM searches the whole image which is inefficient especially for large volume image. In this paper, we propose to combine the 3D Generalized Hough Transform (GHT) and 3D AAM. The 3D GHT can find the center of gravity of kidney efficiently. Then AAM searches around the center of gravity of kidney instead of the whole image. This combination improves the accuracy and efficiency of AAM.

In segmentation of kidney components, the random forests method is used. The random forests method was first proposed

by Breiman [33]. Because of its computational efficiency for handling a huge feature space, it has been widely used in computer vision domain [34]–[40]. M. Yaqub *et al.* [40] argued that the traditional random forests method has two main disadvantages in medical image classification or segmentation: (1) a huge feature pool with many poor features may affect the segmentation accuracy; (2) equal voting by each tree is not the best way to produce classification result. In this paper, feature selection and weighted voting are applied to overcome these problems for kidney component segmentation. Furthermore, we apply the multithreading technology to speed up the segmentation process.

The contributions of this paper are summarized as follows: 1) this is the first framework which can segment kidney into four components; 2) the 3D GHT and 3D AAM method are fully integrated to improve the accuracy and efficiency of traditional AAM; 3) an improved random forests method is used to segment kidney components accurately and efficiently, where both 2D and 3D features are utilized; 4) the proposed method is highly efficient which can segment kidney into four components within 20 seconds.

This paper is organized as follows. In Section II, the complete methodology of localization and segmentation is described. In Section III, a detailed evaluation of this method in terms of its localization and segmentation accuracy on the clinical datasets is presented. The volume change of four kidney components is analyzed in the section. In Section IV, we give our conclusions and discussions.

II. METHOD

The proposed method consists of two phases: localization of renal cortex and segmentation of kidney components. In the localization of renal cortex phase, a method which combines 3D Generalized Hough Transform (GHT) and 3D Active Appearance Models (AAM) is applied to localize the kidney and estimate the thickness of renal cortex. In the segmentation phase, a modified Random Forests (RF) method is proposed to segment the kidney into multiple components based on the result from localization phase. Before the segmentation process, renal cortex thickness table and thick constraint model are built, which are used to help the segmentation of cortex and column. Fig. 2 shows the flowchart of our proposed method.

A. Localization of Renal Cortex

1) *AAM and GHT Training*: During the model building, the anatomical correspondence between training images needs to be established. Since the location and size of the kidney may change considerably from patient to patient, and slice thickness from different CT scanners may differ a lot, in order to get sufficient physical location correspondences between subjects to build 3D AAM [18], [20], interpolation of image slices is needed. During the training stage, the top and bottom slices of kidney are first manually identified. Then linear interpolation is applied to generate the same number of slices for each subject in the training set. Landmarks are manually specified on the inner and outer boundaries of renal cortex for each axial slice.

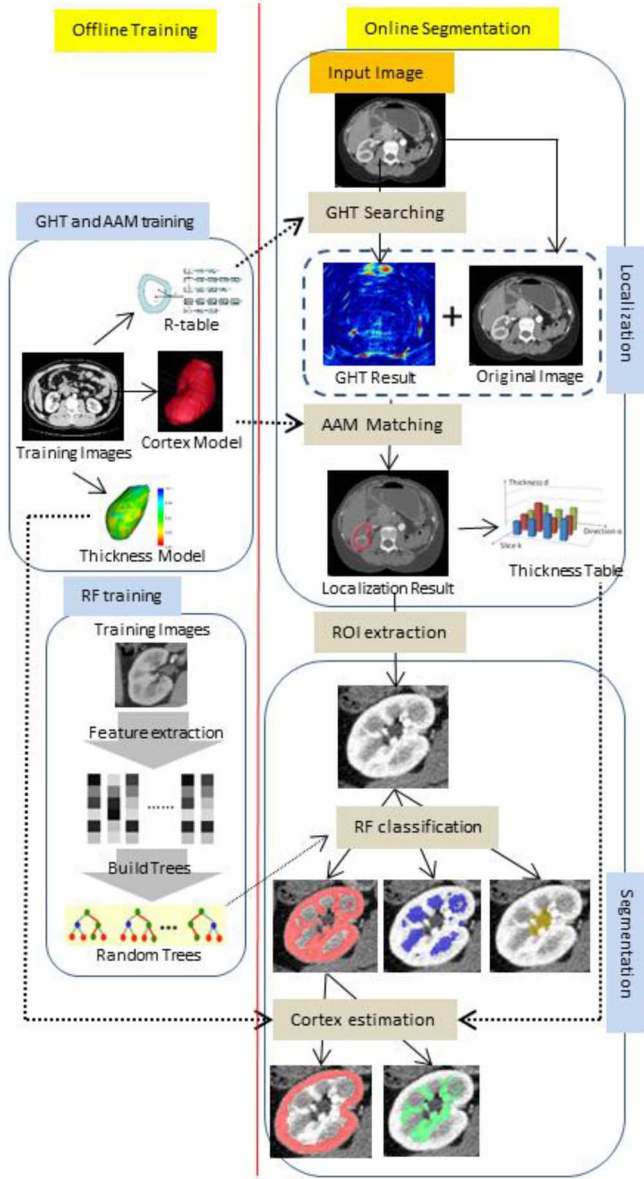


Fig. 2. Flowchart of the proposed method.

The conventional 3D AAM method [41], [42] is applied to construct the renal cortex model. The model includes both shape and texture information.

The mean and standard deviation of thickness of the renal cortex with respect to slice and direction is also computed to construct a renal cortex thickness model, as shown in Fig. 3. This model is used for helping the segmentation of cortex and column in the later stage.

Generalized Hough transform can be used to detect instance of an object with arbitrary shapes, independent of scale and orientation [43], [44]. In GHT, the shape of the target object is stored in a reference table called R-table. Then an accumulator matrix indicating the possible position of the object is constructed according to the R-table. Khoshelham [45] extended this method to detect 3D objects in volumetric data.

In this paper, since the outer surface of kidney (renal cortex) is more distinct, as shown in Fig. 1, this surface is first detected. The outer surface of the mean shape of renal cortex obtained

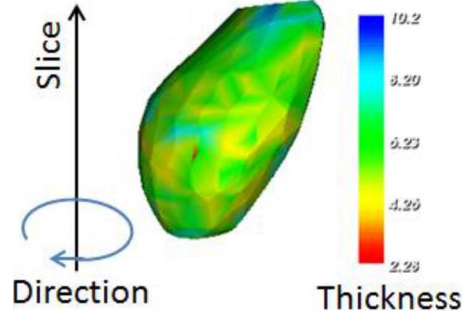


Fig. 3. The mean thickness model of renal cortex.

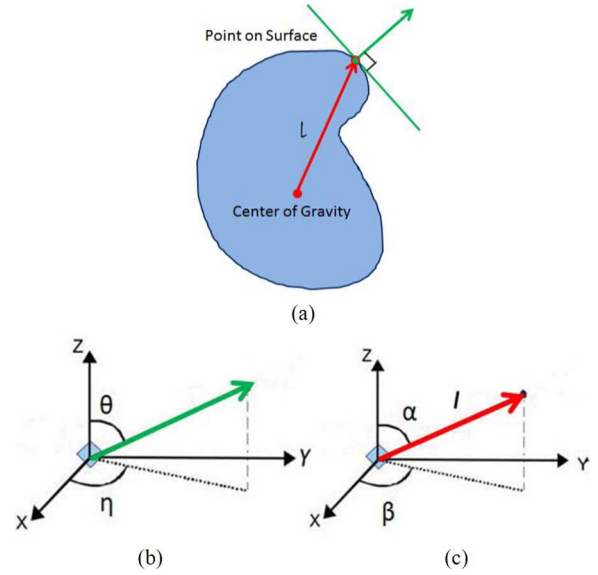


Fig. 4. Parameters involved in the 3D GHT computation. (a) The red arrow shows the vector connecting the center of gravity and an arbitrary point on the surface. The green arrow shows the normal direction of the point on surface; (b) The normal direction of a point on surface is defined by two angles θ and η ; (c) The direction of the vector connecting the surface voxel to the center of gravity is defined by two angles α and β .

by the 3D AAM is stored in the R-table. For every voxel on the outer surface, the surface normal direction, and the length and direction of a vector connecting the surface voxel to the center of gravity are computed as shown in Fig. 4. The surface normal directions are defined by two orientation angles θ and η , which serve as indices in the R-table to look up the length, l , and connecting vector direction, α, β . Fig. 5 illustrates the R-table.

2) *Renal Cortex Localization and Thickness Table Construction*: The localization method is based on a combination of 3D GHT and 3D AAM method. The AAM method matches a new data to the appearance model through minimizing the root mean square (RMS) intensity between the new data and appearance model instance by modifying the affine transformation, global intensity parameters, and appearance coefficients. However, in conventional AAM, the whole volume is searched to obtain an accurate matching, and the computational cost is high. To improve the efficiency, in this paper, the 3D GHT is applied to initialize the searching range by locate the center of gravity of the renal cortex.

Define $P_r(X_r, Y_r, Z_r)$ as a candidate center of gravity of renal cortex, and $P_s(X_s, Y_s, Z_s)$ as a voxel in the test image,

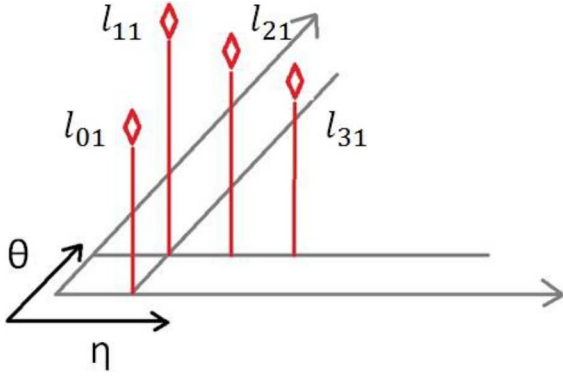


Fig. 5. The illustration of a 3D GHT R-table. The mean outer surface is stored in the R-table. After computing the normal vector of every point on the outer surface, the angles θ and η serve as indices in the R-table to look up the length, l , and connecting vector direction, α .

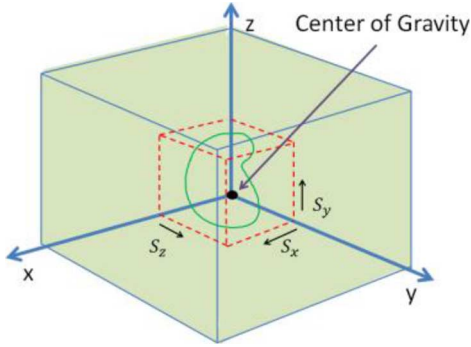


Fig. 6. The illustration of 3D AAM searching area. The outer green cube is the full searching area, while the red dash line shows the restrictive searching area determined by 3D GHT.

if P_s is on the outer surface of renal cortex, their positions satisfy the following equation:

$$\begin{cases} X_r = X_s + 1 \times \sin(\alpha) \times \cos(\beta) \\ Y_r = Y_s + 1 \times \sin(\alpha) \times \cos(\beta) \\ Z_r = Z_s + 1 \times \cos(\beta) \end{cases} \quad (1)$$

A 3D accumulator array with X_r, Y_r, Z_r as the indices is constructed. The normal direction for every voxel in the test image is obtained and used to look up l, α and β in the R-table. Then X_r, Y_r and Z_r are calculated by (1). Each set of X_r, Y_r and Z_r values cast a vote to the corresponding bin in the accumulator array. The bin with the maximum votes indicates the most possible center of gravity of renal cortex, as shown in Fig. 7(b). Because other organs may have the similar shape with kidney, several local maximums could be found. The priori anatomical knowledge is applied to determine which one is the center of gravity of the right kidney. Then 3D AAM is performed in a relative small area around the center of kidney with size $(S_x \times S_y \times S_z)$, as shown in Fig. 6.

Once the localization task is accomplished, the position of the kidney is computed and an initial segmentation of renal cortex is obtained, as shown in Fig. 7(c). The localization results are used to construct a renal cortex thickness table, which help for separation of cortex and column. During this step, first, the center of gravity of kidney is calculated for each slice (m slice). Then n directions are taken evenly around the center of gravity. In each

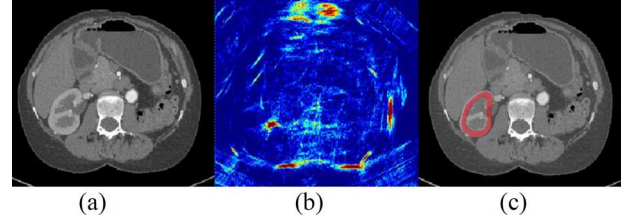


Fig. 7. The illustration of localization step. (a) A testing abdominal CT image. (b) The voting result of GHT, the red color indicates voxels with high possibility as the center of gravity. (c) The result of localization.

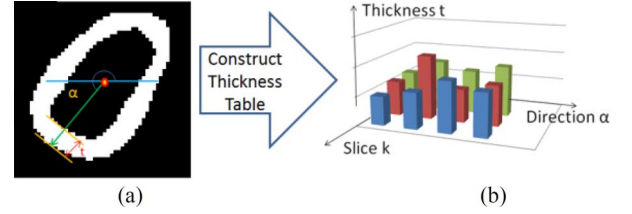


Fig. 8. The illustration of cortex thickness table construction. (a) We calculate the distance t between the outer and inner surface in direction α (the red line is the distance in the current direction). The corresponding α, k and t are saved in thickness table (b).

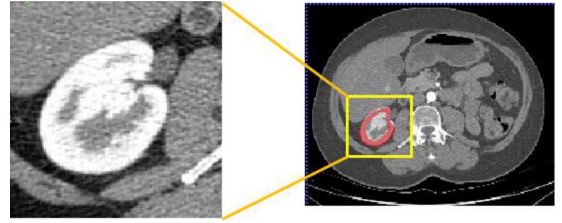


Fig. 9. Extract the Kidney Area From the Original Image.

direction, the distance t between the outer and inner surfaces is calculated as the cortex thickness and stored in the thickness table with size $m \times n$. The slice number k and direction angle α serve as indices in thickness model to lookup thickness t as shown in Fig. 8.

B. Segmentation of Kidney Components

In this part, the kidney will be segmented into four components, renal cortex, renal column, renal medulla and renal pelvis. Before segmentation, the volume of interest for the kidney is extracted based on the localization result, as shown in Fig. 9. During the segmentation, the RF is applied to classify the voxels into four categories: renal cortex/column, renal medulla, renal pelvis and background. The thickness table and thickness constraint model are applied to separate column from cortex.

1) *Features Extraction and Selection*: In this paper, both 2D and 3D features are calculated. The 2D feature set includes: hog features [46], Gabor [47] features, Robert and hessian features. Hog features provide orientation information, Gabor features provide texture information, Robert and Hessian features provide edge information of objects.

The 3D features describe different kinds of relationship between the voxel of interest (VOI) and voxels around it (both intra and inter slice) and help to distinguish voxels with similar intensity and edge information [48]. Table I shows the parameters and description of each feature set (see appendix for more details about the features).

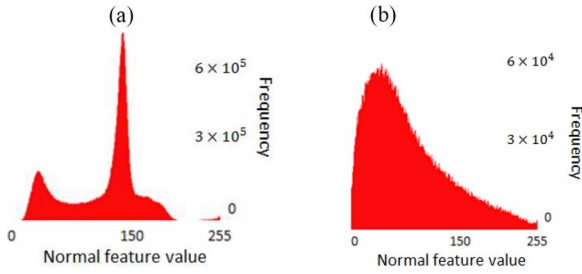


Fig. 10. Histograms of feature values for two feature value extracted from one training image. (a) Histogram of voxel value of Gabor feature extracted from the image. (b) Histogram of voxel value of Hog feature extracted from the image. We find that feature values do not follow normal distribution strictly. (a) Histogram of value of Gabor (b) Histogram of value of Hog feature extracted from the image. We find that feature values do not follow normal distribution strictly.

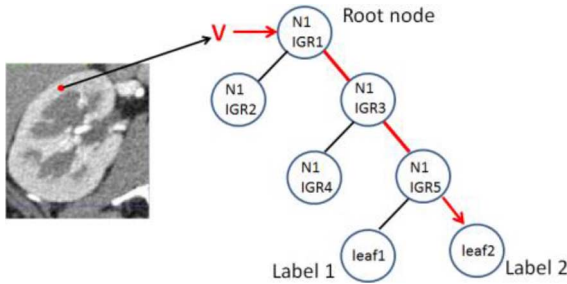


Fig. 11. An unseen voxel (v) starts from the root node and across the trained tree end in a leaf node. The red edges represent the path of v . The score of v in this tree is: $\text{Score}(v) = (\text{IGR1} + \text{IGR3} + \text{IGR5})/3$. This score serves as the weight in our weighted voting RF.

The accuracy of the RF classifier is strongly dependent on the discriminative ability of features. In volumetric images, a huge number of features can be extracted. However, as proved in [40], weak features contribute little to RF classifier decision, or even lead to poor classification results. To overcome this problem, a feature selection phase is needed.

In our work, information gain ratio (IGR) [49] is used as the metric to split a node in RF trees. Features with high IGR are considered as strong features. For each feature, the IGR is calculated as follows:

$$\begin{aligned}
 IGR &= \frac{G(R)}{I(D)} \\
 G(R) &= \text{Info}(D) - \text{Info}_R(D) \\
 \text{Info}(D) &= - \sum_{i=1}^m p_i \log_2(p_i) \\
 \text{Info}_R(D) &= \sum_{j=1}^k \frac{|D_j|}{|D|} \times \text{Info}(D_j) \\
 I(D) &= - \sum_{j=1}^k \frac{|D_j|}{|D|} \times \log_2\left(\frac{|D_j|}{|D|}\right). \quad (2)
 \end{aligned}$$

In which, D is data set, R represents attribute set, and p represents the probability for D . $G(R)$ is information gain. $I(D)$ is split information.

We found from the experiments that only a small number of the features have a high IGR. It means only a few features significantly contribute to RF classification. In this work, 100 best

TABLE I
MAIN PARAMETERS AND FUNCTION OF FEATURE SET.

Feature	Parameters	Description
Gabor	Scale:3,5 with 4 orientation	2D filtering information
Robert	Template size: 2×2	2D edge information
Haar3D	Calculated edge feature template by integral image	3D edge information
Hessian	second order partial derivatives and characteristic value	Shape information
hog	Template size: 3×3; 9 orientations	Orientation information
Average_3D	Block size: 3×3×3; 5×5×5; 9×9×9; 11×11×11	Spatial neighborhood information
Sum_3D	Block size: 3×3×3; 5×5×5; 9×9×9; 11×11×11	Spatial neighborhood information
Binary_3D_diff	Block size: 3×3×3; 5×5×5; 9×9×9; 11×11×11	Spatial neighborhood information
Binary_sum_3D	Block size: 3×3×3; 5×5×5; 9×9×9; 11×11×11	Spatial neighborhood information
Abs_dif_8	Block size: 3×3×3; 5×5×5; 9×9×9; 11×11×11	Spatial neighborhood information

features with the highest IGR are chosen to train the RF trees. This step serves as a preprocessing for the RF training.

2) *Random Forests Training*: As shown in Table I, M ($M = 403$) features are calculated from training data set as the main feature pool. Then N ($N = 100$) features are chosen from the main feature pool as the strong feature pool.

Before training random trees, a parameter F is randomly chosen as the size of features used in building a tree. At the beginning of building each tree, a training example set is randomly chosen [33].

By computing the histogram of features of all data in the training set, we found that they did not follow normal distribution strictly, as shown in Fig. 10. Therefore, we didn't use the threshold picking strategy based on normal distribution [39], but evenly selecting threshold value for our features.

RF is a learning-based technique in which the ground truth of training set was used to build multiple decision trees with a randomized strategy. A decision tree is a tree where each node is a classifier, which splits the training samples into two groups. In tree building, the classifier that maximizes a specific metric, such as IGC, is chosen for each node. A random tree starts from a root node and ends with leaf nodes. Each leaf node contains a likelihood for each class that can be used to generate the classification decision. RF training is a recursive process. The creation of a tree stops when meets two situations: 1) the maximum tree depth is reached; 2) a node split all the current samples into either left child or right child.

To summarize, the RF training is implemented as follows:

Initialization:

Import parameters:

T , tree number; D , max tree depth; G , number of sampling each feature

Calculate parameter: F

Training:

For $i = 1$ to T

Sub_initial:

Random sample with replacement from original data set.

Evenly sample each feature.

Create classifier:

1: Find best score and save current feature, threshold and depth:

For j = 1 to F

For k = 1 to G

Calculate current score

EndFor

EndFor

2. Split current data into left or right according to the feature and threshold.

3. If (left_child = 0 or right_child = 0 or current_depth > D)

Stop

Else

Create classifier with child

Endif

EndFor

3) *Random Forests Classification*: In the RF testing phase, a voxel v of a test image passes through each tree starting from the root node. Once v enters a node, it enters either the left child or the right child according to decision of the current classifier, until it reaches a leaf node, where the probabilistic distribution $p(c_j | v, leaf(tree_t))$ for each class is obtained. In traditional Random Forests, the distributions from all trees are equally combined to form the final decision for classification.

In this paper, a weighted voting mechanism [39] is applied, which outperformed the even voting method in traditional RF [33]. The IGR for each node is a score indicating its classification ability. The mean of scores is calculated in the path as v passes through a tree, as shown in Fig. 11. The voting mechanism is described as follows:

$$\begin{aligned}
 W_t &= \text{Normalized}(\text{Score}(v, tree_t)) \\
 &= \frac{1}{T-1} \left(\frac{\text{Score}(v, tree_t)}{\sum_{t=1}^T \text{Score}(v, tree_t)} \right), \\
 p(c_j | v, RF) &= \sum_{t=1}^T W_t \cdot p(c_j | v, tree_t), \\
 \forall c_j &\in \{c_1, c_2, \dots, c_{label}\}
 \end{aligned} \quad (3)$$

where W_t is the weight for each tree.

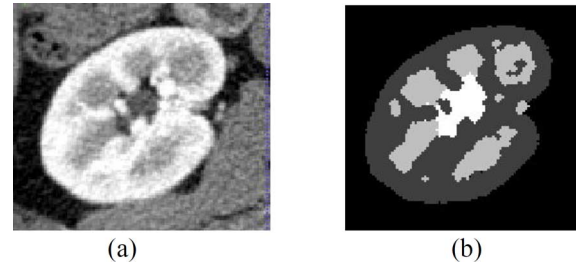


Fig. 12. RF classification result (a) one slice of the original volume data. (b) One slice of RF result.

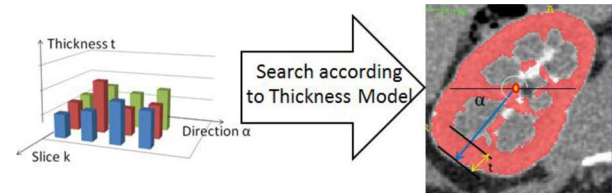


Fig. 13. The illustration of the cortex estimation. We can estimate the thickness t (the yellow line show in right figure) of renal cortex according to the current slice k and direction α in the thickness table.

Fig. 12 illustrates the result of the RF method. To summarize, our RF testing is running as follows:

1. Calculate features for test image

2. Import unseen sample v

3. For $i = 1$ to T

Test(v):

If current node is a leaf node

Stop and return label

Else

If $v.at(\text{node.feature}).value < \text{node.threshold}$

Node.left_child.Test(v)

Else

Node.right_child.Test(v)

Endif

Endif

EndFor

4. Calculate weight

5. Voting and output result

4) *Renal Cortex Segmentation*: In the RF classification, the renal cortex and renal column are considered as one category because their intensity and texture are very similar. Even the experienced expert can hardly separate them accurately. Here, the predefined renal cortex thickness model is used to separate renal column from renal cortex.

As the outer surface of renal cortex is more distinct, the inner surface of renal cortex, i.e., the boundary between cortex and column is calculated by finding the cortex thickness from the

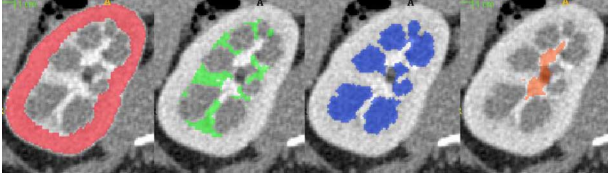


Fig. 14. The results of our segmentation method. The four panels show renal cortex, renal column, renal medulla and renal pelvis respectively.

thickness table. The thickness $T_{k\alpha}$ of current slice k and direction α is first looked up from the thickness table, as shown in Fig. 13, and then corrected by (4).

$$T_{k\alpha} = \begin{cases} u_{k\alpha} - \sigma_{k\alpha}, & \text{if: } T_{k\alpha} < u_{k\alpha} - \sigma_{k\alpha} \\ u_{k\alpha} + \sigma_{k\alpha}, & \text{if: } T_{k\alpha} > u_{k\alpha} + \sigma_{k\alpha} \\ T_{k\alpha}, & \text{else} \end{cases}, \quad (4)$$

where $u_{k\alpha}$ and $\sigma_{k\alpha}$ are the mean and standard deviation of all thickness values in the thickness table. This correction is to prevent large deviation of thickness caused by noise. Once the inner boundary of cortex is decided, the voxels further inside the inner boundary are regarded as renal column. With this method we distinguish cortex from column efficiently.

5) *Post-Processing*: After this process, renal cortex, renal column, renal medulla and renal pelvis as well as background are segmented. Morphological methods are also applied. Opening operation is applied to remove isolated points, followed by closing operation to fill small holes. Both open operation and close operation are implemented only once. The mask size of opening and closing is set as 3×3 . The morphological operations make the segmentation results smooth, but more opening and closing operations or bigger mask can lead to loss of details near boundaries. The result of one slice is shown in Fig. 14.

III. EXPERIMENT AND RESULTS

A. Implementation Detail

1) *Image Dataset and Ground Truth*: Two datasets were used to evaluate the proposed method as follows.

Dataset 1: Abdominal images were acquired during preoperative screening from 27 subjects before kidney donation. Among these 27 subjects, 10 also had contrast-enhanced CT images after nephrectomy.

The dataset was acquired from two different types of CT scanner (GE Medical systems, Light -Speed Ultra, and Philips, Mx8000 IDT 16). The in-plane pixel size ranged from 0.55 to 1 mm. The slices thickness ranged from 1 to 5 mm. In total, we have 37 volume images. Among which, 22 images had slice thickness less than 2.5 mm, 15 images had slice thickness greater than 2.5 mm. The slice number of original abdominal images ranged from 51 to 525. The slice number of kidney area in each abdominal image ranged from 20 to 220.

Dataset 2: Abdominal images were acquired from 5 normal subjects and 5 abnormal subjects. Among the 5 abnormal subjects, they had kidney stone or polycystic kidney.

The dataset was acquired from Siemens SOMATOM sensation 64. The in-plane pixel size ranged from 0.53 to 0.80 mm. The slice thickness ranged from 0.7 to 1 mm. The slice number

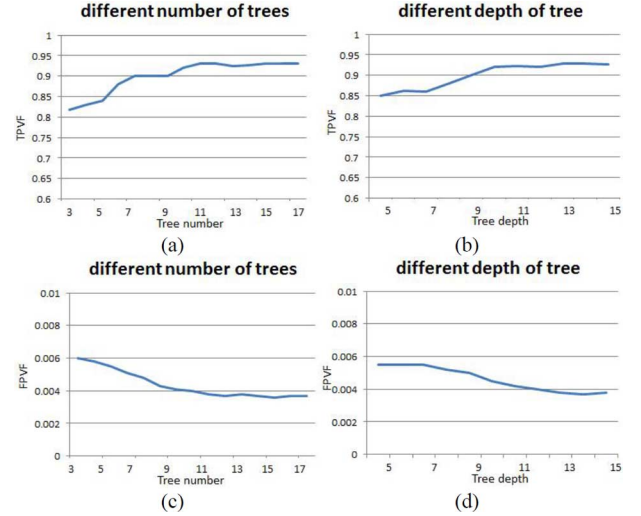


Fig. 15. Mean TPVF/FPVF of renal cortex with different tree number and depth. (a) and (c) Accuracy with different tree number and fixed tree depth 12. (b) and (d) Accuracy with different tree depth and fixed tree number 15. The segmentation accuracy tendency of column, medulla and pelvis are similar.

of original abdominal images ranged from 268 to 360. The slice number of kidney area in each abdominal image ranged from 70 to 100.

Two independent trained observers (user1 and user2) performed manual segmentation as ground truth. Both the observers were experienced radiologic technologists (X. Wang and B. Zhang in the author list). Each observer was blinded to the results of the other. The observers manually drew the kidney components in a slice-by-slice mode using ITK-snap (<http://www.itksnap.org>).

As the training and testing of each tree in RF is independent, we implement RF with multithreading technology. The proposed framework was implemented and tested on a 64-bit system computer (Intel Core i7-3770 CPU, 3.4 GHz and 8 GB RAM).

2) *Parameter Settings*: Before the localization, all the images were interpolated into 32 slices. The size of each testing image was $512 \times 512 \times 32$ after interpolation. In the localization phase, after the center of gravity of kidney is found for a test image by GHT, we set the AAM searching range as $5 \times 5 \times 5$. As shown in Table II, searching range of $10 \times 10 \times 10$ and $2 \times 2 \times 2$ both resulted in larger errors. This was because searching in a large range might give false positive that deviated a lot from the true center of gravity, while searching in a small range might miss the correct point. Moreover, as also shown in the table, searching in the $5 \times 5 \times 5$ range does not cost much more time than the $2 \times 2 \times 2$ case.

For segmentation, the VOI of kidney area was extracted from each test data based on the result of localization phase. We set the VOI size as $128 \times 128 \times 32$, centered around the center of gravity of kidney. The size $128 \times 128 \times 32$ is large enough to contain the whole kidney. In RF segmentation phase, parameters were chosen empirically. $M(403)$ features were calculated as the main feature pool. N best features were selected by the IGR criteria. We set N approximately 25% of $M(N = 100)$. The number of features F used in building a single tree was randomly

selected, as required by the RF method. The number of trees T was set as 15, and the maximum tree depth D was set as 12. In the experiments, larger T and D brought little improvement to the segmentation accuracy. Fig. 15 shows the segmentation accuracy of renal cortex with different T and D . The other components have similar tendency regarding segmentation accuracy.

3) *Methods for Comparison:* Since the proposed method is the first one trying to segment kidney into four parts, it is hard to find related work for comparison. We compare the proposed method with other two methods. 1) Graph cut based method (GC). Graph cut is widely applied in medical image segmentation and its accuracy and robustness have been proved in [51]–[54]. In this method, graph cut is applied to segment the renal cortex and column from the background. For fair comparison, the renal cortex localization is the same with the proposed method. The initial cortex obtained by localization serves as the foreground seed for GC, and the area outside the kidney serves as the background seed. Then threshold is applied to segment renal medulla and renal pelvis. We calculate the average intensity of cortex/column V , then choose $0.5 - 0.7 V$ as the threshold for medulla and $0.3-0.5 V/1.2-1.4 V$ for pelvis. The same cortex thickness model is used to separate renal column from renal cortex.

2) Binary random forest based method (BRF). Note that the graph cut can only segment one target object, while RF can finish multi-target task. To demonstrate the advantages of RF, RF is also used as a binary classifier in this strategy. Renal cortex and renal column are segmented as one part from the background by random forests classifier. The other steps are keeping the same as in GC based method.

We also compare the renal cortex segmentation results of the proposed method with those obtained by the OAM-GC method [25].

Different methods were implemented on Dataset 1 for performance comparison. The proposed method was also tested on Dataset 2 for robustness evaluation.

B. Experimental Results

In this section, we demonstrated both qualitatively and quantitatively the performance of the proposed kidney component segmentation method. We consider manual segmentation performed in this data set to constitute a surrogate of true segmentation for assessing the localization and segmentation accuracy of our methods.

1) *Correlation Evaluation:* The proposed method and manual segmentation have strong correlation, with Pearson's correlations between inter-observer variation (user 1 and user 2), proposed method and user1, proposed method and user2 are: 0.93, 0.92, 0.94 for renal cortex; 0.90, 0.85, 0.82 for renal column; 0.96, 0.92, 0.92 for renal medulla; 0.92, 0.88, 0.90 for renal pelvis. Because the proposed method has a strong correlation with both user1 and user2, the user1 is chosen arbitrary as reference.

2) *Renal Cortex Localization:* The kidney component segmentation method is highly depends on the renal cortex localization step. Our results of renal cortex localization are shown in Fig. 16. To analyze the results quantitatively, the average distance (AD) for kidney centers between ground truth and local-

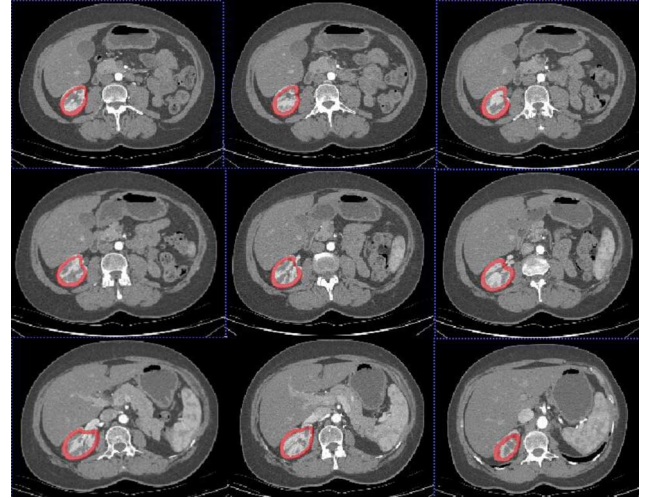


Fig. 16. The experimental result for renal cortex localization is shown in different slice. The original image size is (512×512) .

TABLE II
COMPARISONS BETWEEN 3D AAM AND THE PROPOSED METHOD
(Mean \pm SD)

	Searching area (voxels)	AD(voxels)	Time(seconds)
Conventional 3D AAM	Whole image	12.43 \pm 8.32	40
GHT+AAM	10 \times 10 \times 10	6.05 \pm 2.06	19
	5 \times 5 \times 5	5.42 \pm 3.76	15
	2 \times 2 \times 2	9.07 \pm 7.14	14

ization results, and the running time for the proposed localization method and traditional 3D AAM are used. The AD for the proposed localization method is 5.42 ± 3.76 voxels with the searching area $5 \times 5 \times 5$, while the AD for conventional 3D AAM is 12.43 ± 8.32 (Table II). As shown in Table II, the proposed method has better performance with a shorter running time compared to conventional 3D AAM.

3) *Kidney Component Segmentation:* Since the kidney component segmentation is the key part in the proposed framework, more comprehensive comparison and evaluation are conducted. Fig. 17(a) shows the original image of one particular patient, Fig. 17(b) shows the ground truth and Fig. 17(c) shows the results of the proposed method. All the images have been cropped for the best view. Comparison between different segmentation method and ground truth was shown in Fig. 18. Fig. 19 shows 3D views of the segmentation result by the proposed method.

The results of segmentation part accuracy are expressed in true positive volume fractions (TPVF) and false positive volume fraction (FPVF). The accuracy numbers for the kidney component segmentation is the average accuracy across cases. TPVF indicates the fraction of the total amount of tissue in the true segmentation by the method:

$$TPVF = \frac{|C_{TP}|}{|C_{td}|}. \quad (5)$$

FPVF denotes the amount of tissue falsely identified by the method:

$$FPVF = \frac{|C_{FP}|}{|U_d - C_{td}|}. \quad (6)$$

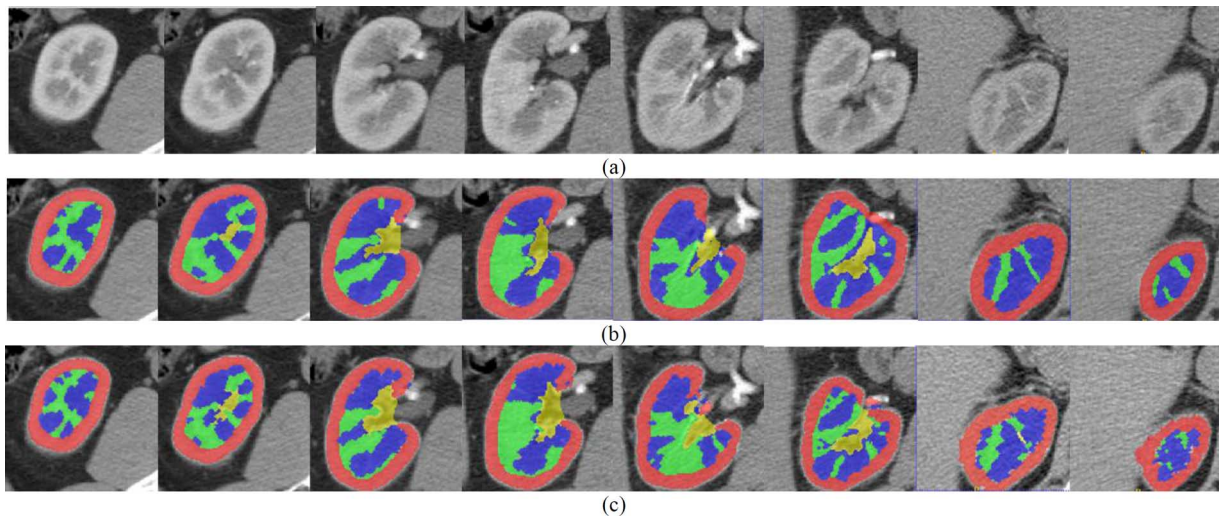


Fig. 17. The experimental results for kidney structures segmentation. Red part represent renal cortex, green part represent renal column, blue part represent renal medulla, while yellow part represent renal pelvis. (a) is original image. (b) is ground truth. (c) is the result of the proposed method.

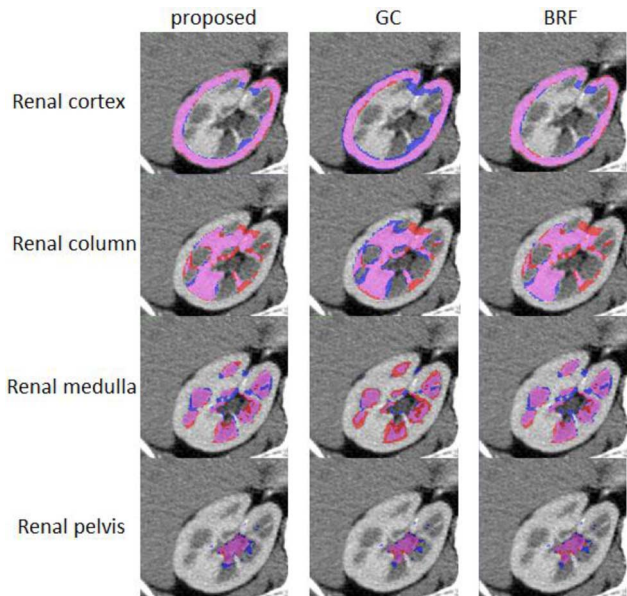


Fig. 18. Comparison between different segmentation method and ground truth. The ground-truth segmentation and auto-method segmentation are overlaid on a single central slice. The red part represents ground truth and blue part represents automatic method. Magenta part is the overlap of ground truth and automatic method.

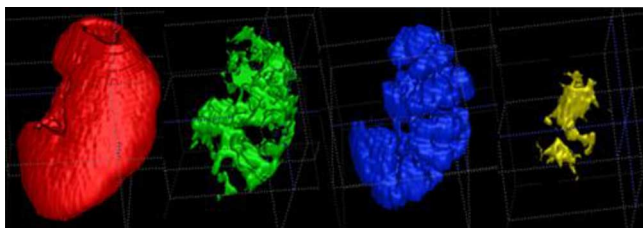


Fig. 19. Renal cortex, renal column, renal medulla and renal pelvis are shown in 3D view respectively.

Where C_{TP} is the set of voxels in the true-positive delineation, C_{td} is the set of voxels in the ground truth, C_{FP} is the set

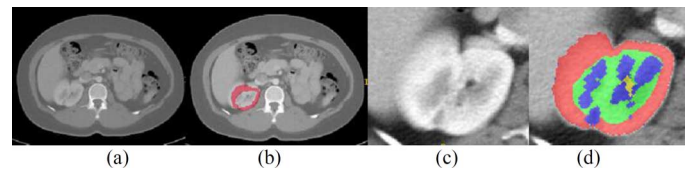


Fig. 20. One case where localization result is poor but segmentation result is good. (a) the original image. (b) the cortex localization result. (c) extracted VOI (d) the segmentation result of kidney components.

of voxels falsely identified, U_d is assumed to be a binary scene with all voxels in the scene domain, and $|\cdot|$ denotes volume. Paired t-tests were used compare the segmentation accuracy and a p-value less than 0.05 was considered statistically significant.

Renal cortex is the most important part in kidney. As shown in Table III, both TPVF and FPVF for renal cortex segmentation of the proposed method ($93.15 \pm 2.21/0.37 \pm 0.16$) are significantly better than GC ($88.85 \pm 2.89/0.64 \pm 0.26$), and OAAM-GC ($90.15 \pm 3.11/0.85 \pm 0.05$). The performance of our method for segmenting renal column, renal medulla and renal pelvis are also better than GC and BRF.

The P-values for paired t-test are shown in Table IV. And the average running time for segmenting one image consisted of localization/initialization and segmentation is shown in Table V, GC and BRF have the same localization step with the proposed method. Compared to GC, BRF and OAAM-GC, the segmentation accuracy of the proposed method gets improved. Moreover, our method is much more computationally efficient.

4) *Robustness Evaluation*: The proposed method consisted of two phase: localization and segmentation. As shown in Table III, we can see that the performance of the later stage (segmentation) get much improved compared to localization stage (the average TPVF/FPVF for renal cortex of localization was 77.23%/0.80%, while of segmentation was 93.15/0.37 based on Dataset 1).

We chose a case in dataset 1 whose localization result was worse to see if the segmentation stage can still segment the kidney into 4 components accurately.

TABLE III
THE SEGMENTATION RESULTS AS TPVF AND FPVF FOR PROPOSED METHOD, GC, BRF AND OAAM-GC ON DATASET 1. (mean \pm std)

	TPVF(%)				
	localization	GC	BRF	OAAM-GC	proposed
cortex	77.23 \pm 10.08	88.85 \pm 2.89	93.09 \pm 2.21	90.15 \pm 3.11	93.15 \pm 2.21
column	-	78.75 \pm 3.83	81.58 \pm 4.26	-	83.09 \pm 4.64
medulla	-	71.50 \pm 13.84	80.73 \pm 10.04	-	81.92 \pm 9.88
pelvis	-	73.21 \pm 9.75	73.21 \pm 9.75	-	80.28 \pm 7.69
	FPVF(%)				
	localization	GC	BRF	OAAM-GC	proposed
cortex	0.80 \pm 0.21	0.64 \pm 0.26	0.34 \pm 0.17	0.85 \pm 0.05	0.37 \pm 0.16
column	-	0.56 \pm 0.36	0.87 \pm 0.52	-	0.97 \pm 0.49
medulla	-	0.71 \pm 0.57	0.61 \pm 0.22	-	0.55 \pm 0.15
pelvis	-	0.16 \pm 0.13	0.15 \pm 0.13	-	0.30 \pm 0.20

TABLE IV
P-VALUES FOR PAIRED T-TEST BETWEEN THE PROPOSED METHOD AND METHODS FOR COMPARISON

	TPVF	
	Proposed/GC	Proposed/BRF
Renal cortex	<0.01	0.02
Renal column	0.04	0.03
Renal medulla	0.04	0.12
Renal pelvis	0.08	0.08
	FPVF	
	Proposed/GC	Proposed/BRF
Renal cortex	0.02	0.15
Renal column	0.02	0.01
Renal medulla	0.2	0.15
Renal pelvis	0.03	0.03

TABLE V
COMPUTATIONAL TIME OF TESTING (SECOND)

	initialization	segmentation
GC	15	35 (for four parts)
BRF	15	10(for four parts)
Proposed method	15	5 (for four parts)
OAAM-GC [17]	40	65 (only for cortex)

As shown in Fig. 20, the kidney localization was not very accurate because of the blurred boundary of the kidney. The distance of kidney centers between ground truth and localization result of this case is 8.83 voxels while the AD (the average distance for kidney centers between ground truth and localization results) is 5.42. The TPVF/FPVF for renal cortex of this case after localization was 67.91%/1.05%.

With this localization result, the segmentation of our proposed method can still segment the kidney into four components as shown in Fig. 20(d). TPVF/FPVF for renal cortex, column, medulla and pelvis of this case by the proposed method were 90.92%/0.74%, 81.87%/1.48%, 78.82%/0.52%, and 72.78%/0.10% respectively.

In order to evaluate the performance of the proposed method on images with different slice thickness, the segmentation results on dataset 1 were separated into two groups based on slice thickness: group 1 (slice thickness < 2.5) and group 2 (slice thickness > 2.5). The quantitative comparison was shown in Table VI and Table VII. As shown in Table VI the proposed method can segment kidney into 4 components accurately on images with different slice thickness. The p-values in

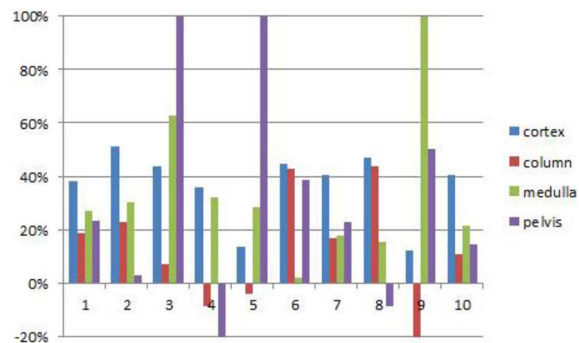


Fig. 21. Kidney components volume change of each case by the proposed method.

Table VII shows that the segmentation results of our proposed method did not have statistically significantly difference on images with different slice thickness except for cortex.

The robustness of the proposed method was also tested on different dataset from different CT system. We trained using Dataset 1, and then tested on Dataset 2. Because the slice thickness differs a lot from different CT system, linear interpolation was implemented as described in Section II. The segmentation results expressed as TPVF and FPVF (mean \pm std) are shown in Table VIII. As shown in this experiment, the proposed method can segment kidney into four components for different datasets accurately.

5) *Volume Change of Kidney Components*: By the proposed method, the volume change of the four components of the remaining kidney before and after kidney donation can be calculated. For the 10 donors with both preoperative and postoperative CT scans, the cortex, column, medulla and pelvis volume of the remaining kidney were 82.8 \pm 12.8 mL, 35.6 \pm 7.3 mL, 44.9 \pm 6.8 mL, 3.5 \pm 1.6 mL before donation, respectively; and 111.9 \pm 9.9 mL, 38.7 \pm 5.4 mL, 59.9 \pm 10.8, 4.8 \pm 1.7 mL after donation, respectively. The mean volume change of renal cortex, column, medulla and pelvis were 35.1%, 8.5%, 33.4% and 35.8% increasing, respectively. Fig. 21 shows the volume change of four kidney components of each case. The volume of four kidney components increased in most cases. The increase of renal cortex and medulla volume was statistically significant, as shown in Table IX. In 3 cases, one component (column or pelvis) volume decreased after donation. And in only one case, both column and pelvis volume decreased. The volume change

TABLE VI
THE SEGMENTATION RESULTS AS TPVF AND FPVF FOR PROPOSED METHOD ON THE TWO GROUPS OF DATASET 1. (mean \pm std)

	Dataset 1			
	Slice thickness < 2.5		Slice thickness > 2.5	
	TPVF	FPVF	TPVF	FPVF
cortex	94.75 \pm 1.43	0.33 \pm 0.06	91.16 \pm 1.13	0.42 \pm 0.21
column	83.99 \pm 5.80	0.97 \pm 0.41	81.85 \pm 1.96	0.96 \pm 0.53
medulla	85.79 \pm 7.58	0.48 \pm 0.15	77.09 \pm 10.28	0.64 \pm 0.08
pelvis	80.96 \pm 9.11	0.27 \pm 0.12	79.78 \pm 5.37	0.35 \pm 0.23

TABLE VII
P-VALUES FOR TWO-SAMPLE T-TEST BETWEEN THE SEGMENTATION RESULTS OF KIDNEY COMPONENTS FOR GROUP 1 (Slice thickness < 2.5) AND GROUP 2 (Slice thickness > 2.5)

	TPVF	FPVF
cortex	0.04	0.25
column	0.35	0.48
medulla	0.11	0.06
pelvis	0.44	0.29

of kidney components especially for renal cortex was closely related to kidney function recovery [29].

IV. CONCLUSION AND DISCUSSION

In this paper, we proposed a fast fully automatic method for kidney components segmentation. The proposed method consists of two main parts: localization of renal cortex and segmentation of kidney components. In the localization phase, a fast localization method which effectively combines 3D GHT and 3D AAM is proposed, which utilizes the global shape and texture information. In the segmentation phase, a modified RF method and a cortex thickness model are proposed to efficiently accomplish the multi-structure segmentation task. The proposed method was tested on a CT dataset comprised of 37 images.

To the best of our knowledge, this framework is the first one trying to segment kidney into four components. In this paper, we combined 3D GHT and 3D AAM effectively, which is much more accurate and efficient than the conventional AAM: 5.420 ± 3.761 voxels versus 12.435 ± 8.324 voxels for accuracy, 15 seconds versus 33 seconds for efficiency. The improved random forests method makes use of both 2D and 3D features to segment kidney components accurately and efficiently. With multi-thread technology, the whole workflow for segmenting one test image is highly efficient, which took only 20 seconds.

In this paper, we have compared the proposed method to GC, BRf and GC-OAAM. GC method depends on foreground seed and background seed which often require manual input. In GC-OAAM, the OAAM method which combines live wire [50] and AAM to improve the segmentation performance, however, live wire is difficult to extend to 3D. Therefore, OAAM is a 2D method which cannot make use of the context information among slices. Comparing to above methods, the proposed method is a real 3D and fully automatic method. The proposed method consists of two main parts: localization and segmentation. For localization, it is based on 3D GHT and AAM, which is fully automatic. For segmentation, the modified RF method

does not require seeds input, which is also automatic. And it utilizes 3D spatial information. Thus, the proposed framework is a 3D fully automatic method, which overcomes problems existing in GC and GC-OAAM method. As shown in Tables III–V, both TPVF and FPVF of the proposed method are improved compared to the GC, BRf and OAAM-GC. Hence, efficiency of the proposed method is improved compared to GC and GC-OAAM. Moreover, the proposed method is also more efficient. The localization and segmentation cost only 15 second and 5 seconds, while for the GC-OAAM, initialization, kidney segmentation, and cortex segmentation costs 40 seconds, 35 seconds and 30 seconds, respectively.

It is important to notice that the segmentation results for renal pelvis are not as good as other kidney components, which may be due to the following reasons: 1) the renal pelvis consists of different issues which have different intensities; 2) the shape of renal pelvis varies a lot; 3) the renal pelvis extends out of the kidney and is connected to other organs. Further investigations will be explored in the near future.

Our proposed method can segment kidney into four components accurately and efficiently. Volume and structure change of each component (renal cortex, column, medulla and pelvis) in kidney can be analyzed by the proposed method based on CT images, while most existed methods only analyzed volume and morphology of whole kidney or renal cortex. The correlation between volumes of kidney components and other biomarkers like serum creatinine [28], glomerular filtration rate (GFR) [55] and effective renal plasma flow (ERPF) [55] can be analyzed. The Serum creatinine, GFR and ERPF are important biomarkers to evaluate kidney function. The correlation between volume of kidney and these biomarkers can provide both kidney anatomy and function information. It is important for clinical application, such as evaluation of potential kidney donors [11] and prediction of recipient renal function [28]. Disease diagnosis, post-operative assessment and other clinical application can benefit from our proposed method. Beside kidney segmentation, our proposed method can be also used to segment other organ with complex structure, such as heart and brain.

Currently the proposed algorithm works well for kidneys whose structures are not significantly altered by diseases. If diseases such as kidney tumor causes dramatic change in kidney morphology or texture, our modified AAM which are trained on the normal dataset may not perform well. For renal cortex and column segmentation, the renal cortex thickness model is also designed for normal cortex shape. A more flexible cortex model will be developed in the near future. For random forest classification, to segment kidney with significant change in

TABLE VIII
THE SEGMENTATION RESULTS AS TPVF AND FPVF FOR PROPOSED METHOD ON DATASET 2. (mean \pm std)

	Dataset 2			
	normal		abnormal	
	TPVF	FPVF	TPVF	FPVF
cortex	92.40 \pm 0.48	0.52 \pm 0.20	90.15 \pm 0.56	0.51 \pm 0.29
column	85.10 \pm 2.47	0.60 \pm 0.20	83.32 \pm 0.88	0.81 \pm 0.23
medulla	83.95 \pm 0.82	0.53 \pm 0.25	81.33 \pm 4.74	0.60 \pm 0.17
pelvis	70.91 \pm 8.67	0.10 \pm 0.05	75.74 \pm 2.55	0.12 \pm 0.05

TABLE IX
P-VALUES FOR PAIRED T-TEST BETWEEN THE KIDNEY COMPONENTS VOLUME BEFORE AND AFTER DONATION

	Volume change
Renal cortex	<0.01
Renal column	0.1
Renal medulla	<0.01
Renal pelvis	0.04

morphology or texture, training on specific dataset is also desired. Another limitation of the proposed method is all images used in this paper were contrast-enhanced. The segmentation task is more difficult for non-contrast-enhanced CT images.

REFERENCES

- [1] Summary Health Statistics for U.S. Adults: National Health Interview Survey [Online]. Available: <http://www.nlm.nih.gov/medlineplus/kidneydiseases>
- [2] Deaths: Final Data for 2010 [Online]. Available: <http://www.nlm.nih.gov/medlineplus/kidneydiseases>
- [3] W. L. Clapp, "Renal anatomy," in *Silva's Diagnostic Renal Pathology*, X. J. Zhou, Z. Laszik, T. Nadasdy, V. D. D'Agati, and F. G. Silva, Eds. New York: Cambridge Univ. Press, 2009.
- [4] S. Stefan *et al.*, "Efficacy and safety of tachosil as haemostatic treatment versus standard suturing in kidney tumour resection: A randomised prospective study," *Eur. Urol.*, vol. 52, no. 4, pp. 1156–1163, 2007.
- [5] L. Jun, Z. Xiaodong, and L. Erping, "Study on differential diagnosis of renal column hypertrophy and renal tumors by pulsed subtraction contrast-enhanced ultrasonography," *Chin. J. Ultrasound Med.*, 2006.
- [6] T. Hart *et al.*, "Mutations of the UMOD gene are responsible for medullary cystic kidney disease 2 and familial juvenile hyperuricaemic nephropathy," *J. Med. Genetics*, vol. 39, no. 12, pp. 882–892, 2002.
- [7] J. Bennington and J. Beckwith, *Tumors of the Kidney, Renal Pelvis, and Ureter*. Washington, DC: Armed Forces Inst. Pathol., 1975.
- [8] O. Gloger *et al.*, "Fully automated renal tissue volumetry in MR volume data using prior shape based segmentation in proband-specific probability maps," *IEEE Trans. Biomed. Eng.*, vol. 62, no. 10, pp. 2338–2351, Oct. 2015.
- [9] M. D. Beland, N. L. Walle, J. T. Machan, and J. J. Cronan, "Renal cortical thickness measured at ultrasound: Is it better than renal length as an indicator of renal function in chronic kidney disease?," *Am. J. Roentgenol.*, vol. 195, no. 2, pp. 146–149, 2010.
- [10] N. S. Muto *et al.*, "Renal cortical volume measured using automatic contouring software for computed tomography and its relationship with BMI, age and renal function," *Eur. J. Radiol.*, vol. 78, no. 1, pp. 151–156, 2011.
- [11] F. Artunc *et al.*, "Simultaneous evaluation of renal morphology and function in live kidney donors using dynamic magnetic resonance IMAGING," *Nephrol. Dial. Transplant.*, vol. 25, no. 6, pp. 1986–1991, 2010.
- [12] L. A. Stevens, J. Coresh, T. Greene, and A. S. Levey, "Assessing kidney function—Measured and estimated glomerular filtration rate," *N. Eng. J. Med.*, vol. 354, no. 23, pp. 2473–2483, 2006.
- [13] C. Mounier-Vehier *et al.*, "Cortical thickness: An early morphological marker of atherosclerotic renal disease," *Kidney Int.*, vol. 61, no. 2, pp. 591–598, 2002.
- [14] S. A. Koff *et al.*, "Renal pelvis volume during diuresis in children with hydronephrosis: Implications for diagnosing obstruction with diuretic renography," *J. Urol.*, vol. 174, no. 1, pp. 303–307, 2005.
- [15] J. A. d. Priester *et al.*, "MR renography by semiautomated image analysis: Performance in renal transplant recipients," *J. Magn. Reson. Imag.*, vol. 14, pp. 134–140, 2001.
- [16] W. Shen, A. A. Kassim, H. K. Koh, and B. Shuter, "Segmentation of kidney cortex in MRI studies: A constrained morphological 3D h-maxima transform approach," *Int. J. Med. Eng. Informat.*, vol. 1, no. 3, pp. 330–341, 2009.
- [17] B. Chevallier, Y. Ponvianne, J. L. Collette, M. Claudon, and O. Pietquin, "Functional semi-automated segmentation of renal DCE-MRI sequences," *ICASSP*, pp. 525–528, 2008.
- [18] H. Shim *et al.*, "Semiautomated segmentation of kidney from high-resolution multidetector computed tomography images using a graph-cuts technique," *J. Comput. Assist. Tomogr.*, vol. 33, no. 6, pp. 893–901, 2009.
- [19] M. Freiman, A. Kronman, S. J. Esses, L. Joskowicz, and J. Sosna, "Non-parametric iterative model constraint graph min-cut for automatic kidney segmentation," in *Proc. MICCAI 2010*, 2010, pp. 73–80.
- [20] D. T. Lin, C. C. Lei, and S. W. Hung, "Computer-aided kidney segmentation on abdominal CT images," *IEEE Trans. Inf. Technol. Biomed.*, vol. 10, no. 1, pp. 59–65, Jan. 2006.
- [21] A. M. Ali, A. A. Farag, and A. S. El-Baz, "Graph cuts framework for kidney segmentation with prior shape constraints," *Proc. MICCAI*, pp. 384–392, 2007.
- [22] Y. Tang, H. A. Jackson, R. E. De Filippo, M. D. Nelson, and R. A. Moats, "Automatic renal segmentation applied in pediatric MR urography," *Int. J. Intell. Inform. Process.*, vol. 1, no. 1, pp. 12–19, 2010.
- [23] J. Xie, Y. Jiang, and H. Tsui, "Segmentation of kidney from ultrasound images based on texture and shape priors," *IEEE Trans. Med. Imag.*, vol. 24, no. 1, pp. 45–57, Jan. 2005.
- [24] R. Cuingnet *et al.*, "Automatic detection and segmentation of kidneys in 3D CT images using random forests," in *Medical Image Computing and Computer-Assisted Intervention-MICCAI 2012*. Berlin, Germany: Springer, 2012, pp. 66–74.
- [25] X. Chen *et al.*, "An automatic method for renal cortex segmentation on CT images," *Acad. Radiol.*, vol. 19, pp. 562–570, 2012.
- [26] S. Will *et al.*, "Automated segmentation and volumetric analysis of renal cortex, medulla, and pelvis based on non-contrast-enhanced T1- and T2-weighted MR images," *Magn. Reson. Mater. Phys., Biol. Med.*, vol. 27, no. 5, pp. 445–454, 2014.
- [27] X. Yang *et al.*, "Automatic segmentation of renal compartments in DCE-MRI images," in *Medical Image Computing and Computer-Assisted Intervention 2015*. Berlin, Germany: Springer, 2015, pp. 3–11.
- [28] C. M. Hugen *et al.*, "Size does matter: Donor renal volume predicts recipient function following live donor renal transplantation," *J. Urol.*, vol. 185, pp. 605–609, 2011.
- [29] H. G. Jeon *et al.*, "Predictors of kidney volume change and delayed kidney function recovery after donor nephrectomy," *J. Urol.*, vol. 184, pp. 1057–1063, Sep. 2010.
- [30] T. F. Cootes, G. J. Edwards, and C. J. Taylor, "Active appearance models," in *Proc. Eur. Conf. Comput. Vis.*, H. Burkhardt and B. Neumann, Eds., 1998, vol. 2, pp. 484–498.
- [31] J. Xiao, J. Chai, and T. Kanade, "A closed-form solution to non-rigid shape and motion recovery," *Proc. ECCV*, 2004.
- [32] S. C. Mitchell *et al.*, "Multistage hybrid active appearance model matching: Segmentation of left and right ventricles in cardiac MR images," *IEEE Trans. Med. Imag.*, vol. 20, no. 5, pp. 415–423, May 2001.
- [33] L. Breiman, "Random forests," *Mach. Learn.*, vol. 45, no. 1, pp. 5–32, 2001.
- [34] H. Deng and G. Runger, "Gene selection with guided regularized random forest," *Pattern Recognit.*, vol. 46, no. 12, pp. 3483–3489, 2013.
- [35] J. Gall *et al.*, "Hough forests for object detection, tracking action recognition," *IEEE Trans. Pattern Anal. Mach. Intell.*, vol. 33, no. 11, pp. 2188–2202, Nov. 2011.

- [36] J. Shotton, M. Johnson, and R. Cipolla, "Semantic texton forests for image categorization and segmentation," in *Proc. IEEE CVPR Conf.*, 2008, pp. 1–8.
- [37] V. Lepetit and P. Fua, "Keypoint recognition using randomized trees," *IEEE Trans. Pattern Anal. Mach. Intell.*, vol. 28, no. 9, pp. 1465–1479, Sep. 2006.
- [38] R. Cuingnet *et al.*, "Automatic detection and segmentation of kidneys in 3D CT images using random forests," *Proc. MICCAI*, vol. 7512, pp. 66–74, 2012.
- [39] V. Lempitsky, M. Verhoeke, J. A. Noble, and A. Blake, "Random forest classification for automatic delineation of myocardium in real-time 3-D echocardiography," in *Proc. 5th Int. Conf. Funct. Imag. Model. Heart*, 2009.
- [40] M. Yaqub, M. Javaid, C. Cooper, and J. Noble, "Investigation of the role of feature selection and weighted voting in random forests for 3-D volumetric segmentation," *IEEE Trans. Med. Imag.*, vol. 33, no. 2, pp. 258–271, Feb. 2014.
- [41] S. Mitchell *et al.*, "3-D active appearance models: Segmentation of cardiac MR and ultrasound images," *IEEE Trans. Med. Imag.*, vol. 21, no. 9, pp. 1167–1178, Sep. 2002.
- [42] M. Stegmann, B. Ersbll, and R. Larsen, "FAME—a flexible appearance modeling environment," *IEEE Trans. Med. Imag.*, vol. 22, no. 10, pp. 1319–1331, Oct. 2003.
- [43] D. H. Ballard, "Generalizing the Hough transform to detect arbitrary shapes," *Pattern Recognit.*, vol. 13, no. 2, pp. 111–122, 1981.
- [44] M. Chang, I. Kim, and J. Park, "Optical flow measurement based on Boolean edge detection and Hough transform," *Int. J. Control, Automat., Syst.*, vol. 1, no. 1, pp. 119–126, Mar. 2003.
- [45] K. Khoshelham, "Extending generalized houghtransform to detect 3D objects in laser range data," in *ISPRS Workshop on Laser Scanning 2007 and SilviLaser 2007*, Espoo, Finland, Sep. 12–14, 2007.
- [46] C. Chen and G. Zheng, "Fully automatic segmentation of AP pelvis X-rays via random forest regression and hierarchical sparse shape composition," *Comput. Anal. Images Patterns*, vol. 8047, pp. 335–343, 2013.
- [47] T. S. Lee, "Image representation using 2D Gabor wavelets," *IEEE Trans. Pattern Anal. Mach. Intell.*, vol. 18, no. 10, pp. 959–971, Oct. 1996.
- [48] M. Yaqub *et al.*, "Weighted voting in 3D random forest segmentation," *Proc. Med. Image Understand. Anal.*, pp. 261–266, 2010.
- [49] J. Dai and Q. Xu, "Attribute selection based on information gain ratio in fuzzy rough set theory with application to tumor classification," *Appl. Soft Comput.*, vol. 13, no. 1, pp. 211–221, 2013.
- [50] A. Falcao *et al.*, "User-steered image segmentation paradigms: Live wire and live lane," *Graph Models Image Process.*, vol. 60, pp. 233–260, 1998.
- [51] X. Chen and U. Bagci, "3D automatic anatomy segmentation based on iterative graph-cut-ASM," *Med. Phys.*, vol. 38, no. 8, Aug. 2011.
- [52] X. Chen *et al.*, "Three-dimensional segmentation of fluid-associated abnormalities in retinal OCT: Probability constrained graph-search-graph-cut," *IEEE Trans. Med. Imag.*, vol. 31, no. 8, pp. 1521–1531, 2012.
- [53] X. Chen *et al.*, "Medical image segmentation by combining graph cuts and oriented active appearance models," *IEEE Trans. Image Process.*, vol. 21, no. 4, pp. 2035–2046, Apr. 2012.
- [54] F. Shi *et al.*, "Automated 3-D retinal layer segmentation of macular optical coherence tomography images with serous pigment epithelial detachments," *IEEE Trans. Med. Imag.*, vol. 34, no. 2, pp. 441–452, Feb. 2015.
- [55] P. Weidmann *et al.*, "Blood levels and renal effects of atrial natriuretic peptide in normal man," *J. Clin. Invest.*, vol. 77, no. 3, p. 734, 1986.